Sinusoidal Frequency-Modulated Waveforms Generated by a Phase-Modulated Frequency-Shifting Loop

Hongzhi Yang, Lei Wang, Changming Zhao, and Haiyang Zhang

***Abstract*—We theoretically and experimentally investigate a phase-modulated frequency-shifting loop (PM-FSL) that includes an electro-optic phase modulator (EOPM) and a gain element, and is seeded by a single-frequency laser. By slightly detuning the modulation frequency of the EOPM off an integer multiple of the fundamental loop frequency, we generate an output waveform that exhibits a series of pulse doublets modulated at radio frequency (RF). We prove that the series consists of sinusoidal frequency-modulated (SFM) pulse doublets whose repetition rate and bandwidth are easily reconfigurable. We report the generation of the SFM waveforms with bandwidth above 7 GHz (limited by the detection bandwidth) by simply tuning the input RF tone over a span of a few kHz in the vicinity of 14.58 MHz (the round-trip frequency). The system is modeled using a time-delayed interference model that accounts for the modulation function of the EOPM, the loop delay time, and the detuning parameter. The model explains the formation of SFM pulse doublets and effectively reproduces all the experimental waveforms. This well-defined waveform may find applications in RF-optical signal processing and radar systems.**

***Index Terms*—Electro-optic phase modulation, frequency shifting loop, sinusoidal frequency-modulated pulse doublets.**

I. Introduction

WAVEFORMS whose instantaneous frequency or phase varies nonlinearly with time are of primary importance for applications such as pulse compression radar [1], radio-frequency (RF) signal processing [2]–[3] and communications [4]. In contrast to the case of linear frequency modulation, pulse compression radar with nonlinear frequency modulation does not require amplitude weighting for the suppression of the resulting sidelobes, and filter adjustment with much steeper edges but nevertheless low time-sidelobes becomes possible [5]–[6]. In this way, the losses in the signal-to-noise ratio that would otherwise occur due to amplitude weighting are avoided. Moreover, nonlinear modulation techniques, such as techniques involving wideband phase-modulated waveforms, are also widely used in various communication contexts, such as broadcasting, satellite communications, and cellular telephone systems, to benefit from the corresponding robust anti-noise performance. However, traditional electronic devices suffer from limited bandwidths with high noise at high frequencies. Compared with traditional electronic methods, photonic generation methods present an attractive alternative, offering high precision, ultrawide bandwidths and low noise [7]–[9]. Over the past decades, the scientific community has conducted extensive research towards the development of efficient photonics-based sources of frequency-modulated (FM) signals. Numerous approaches have been proposed, including space-to-time mapping [10]–[11], Fourier transform pulse shaping [12]–[14], and optical heterodyning [15]–[16]. The first two techniques have been demonstrated to be viable means of generating FM waveforms. By appropriately designing the frequency response of a spatial light modulator or a fiber-optic spectral filter, an electrical pulse of the same shape as the shaped spectrum can be obtained after frequency-to-time mapping. In addition, frequency-shifting loops (FSLs) based on acousto-optic frequency shifters (AOFSs) have been shown to produce broadband chirped waveforms [17] and have been applied for laser ranging [18]–[20].

An FSL usually relies on the use of an AOFS [21]–[22]. However, while they feature high frequency conversion efficiency in the sub-100 MHz range, AOFSs suffer from limited bandwidths (MHz) and tunability. By contrast, an electro-optic modulator (EOM) can offer a much higher bandwidth, e.g., a few tens of GHz. Recently, FSLs based on EOMs have been proposed in different contexts, either for real-time Fourier transformation, or for high-speed optical transmission. For optical real-time Fourier transformation, a "mirror effect" frequency-to-time mapping property based on a phase-modulated FSL was theoretically demonstrated [23]. For high-speed optical transmission, a multicarrier source with high power flatness and stability was built to achieve transmission rates as high as Tb/s [24]. Moreover, similar setups have been shown to produce pulse doublets in the integer Talbot condition [25] and pulse repetition rate enhancement or a fractional Talbot laser [26]. In our work, we further investigate a phase-modulated frequency-shifting loop (PM-FSL) in which a common electro-optic phase modulator (EOPM) replaces the AOFS. We focus on the small detuning

Manuscript received November 1, 2020; revised January 6, 2021 and January 25, 2021; accepted February 12, 2021. Date of publication February 17, 2021; date of current version May 16, 2021. This work was supported by the Qian Xuesen Laboratory under Grant Y-KC-WY-99-ZY-000-020. *(Corresponding authors: Lei wang.)*

Hongzhi Yang and Lei Wang are with the Qian Xuesen Laboratory of Space Technology, Beijing 100094, China (e-mail: yanghongzhi@qxslab.cn; wanglei@qxslab.cn).

Changming Zhao is with the School of Optics and Photonics, Beijing Institute of Technology, Beijing 100811, China (e-mail: zhaochangming@bit.edu.cn).

Haiyang Zhang is with the School of Optics and Photonics, Beijing Institute of Technology, Beijing 100811, China (e-mail: ocean@bit.edu.cn).

Color versions of one or more figures in this article are available at https://doi.org/10.1109/JLT.2021.3059875.

Digital Object Identifier 10.1109/JLT.2021.3059875

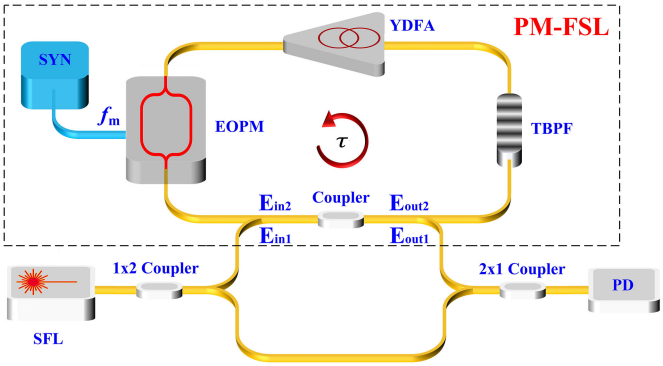

Fig. 1. Sketch of the PM-FSL. SFL: single-frequency laser; SYN: synthesizer; TBPF: tunable bandpass filter; YDFA: ytterbium-doped fiber amplifier; EOPM: electro-optic phase modulator; PD: photodiode.

case in which the modulation frequency is slightly detuned off an integer multiple of the fundamental loop frequency. Instead of the integer or the fractional Talbot condition, the small detuning frequency will destroy the constructive interference of the frequency-shifted laser, which raises questions about the ability to generate sinusoidal frequency-modulated waveforms. Furthermore, an analytical model has to be derived in order to take into account the detuning frequency.

This paper is organized as follows. In Section II, we present an analytical model of the PM-FSL field. Then, we consider a special case in which the modulation frequency is slightly detuned off an integer multiple of the fundamental loop frequency. In the third section, we derive an expression for the resulting electric field and theoretically indicate that it generates sinusoidal frequency-modulated pulse doublets. We characterize the properties of the pulse doublets with respect to the detuning frequency and the optical frequency of the seed laser. The fourth section presents the experimental results obtained with standard components at 1.064 μm, focusing on the influence of modulating frequency on the PM-FSL properties. The output waveforms are investigated by tuning the input RF tone over a span of a few kHz in the vicinity of the integer Talbot condition. Finally, we discuss possible extensions of this work.

II. Continuous-Wave-Seeded PM-FSL

We consider a PM-FSL characterized by a round-trip time of $\tau = 1/f_c$, as depicted in Fig. 1. It is seeded by a single-frequency laser (SFL). The simple architecture of the SFL-seeded FSL includes an EOPM to induce a dual-sideband frequency shift f_m per round trip, a gain medium to compensate for losses, and an optical bandpass filter to serve as a spectral filter. A 2×2 coupler enables seeding the loop and extracting a fraction of the circulating laser power.

To predict the output waveform, we derive a multifrequency time-delayed interference model. Given the transmission matrix $[t_{ij}]$ of the 2×2 coupler and the electric field $E_{in}e^{-j\omega_o t}$ of the seed laser, the output field extracted from the circulating loop can be written as follows:

$$\begin{bmatrix} E_{out1}(t) \\ E_{out2}(t) \end{bmatrix} = \begin{bmatrix} t_{11} & t_{12} \\ t_{21} & t_{22} \end{bmatrix} \begin{bmatrix} E_{in1}(t) \\ E_{in2}(t) \end{bmatrix} \tag{1}$$

Suppose that the modulation function of the phase modulator can be modeled as $\Upsilon(t - n\tau) = e^{j\delta \sin(2\pi f_m(t-n\tau))}$ for round trip n, where δ is the modulation depth and f_m is the modulation frequency. The modulation depth $\delta = \pi V/V_\pi$ depends on the RF voltage V and the half-wave voltage V_π. Let η and G denote the intensity loss of the loop and the intensity gain parameter, respectively; then, if we adopt the notation $\gamma = \sqrt{\eta G}$, since $E_{in2}(t) = \gamma E_{out2}(t-\tau)\Upsilon(t-\tau)$, the electric field at output port 1 of the 2×2 coupler can be expressed as

$$E_{out1}(t) = \left(t_{11} + \frac{t_{21}t_{12}}{t_{22}} \sum_{l=1}^{N} p^l e^{jl\omega_o\tau} \prod_{n=1}^{l} e^{j\delta \sin(2\pi f_m(t-n\tau))}\right) E_{in}e^{-j\omega_o t} \tag{2}$$

where $p = t_{22}\,\gamma$ is the overall amplitude transmission coefficient. We define N as the largest possible integer number of round trips, which is determined by t_{22} and γ. $\prod_{n=1}^{l} exp[j\delta \sin(2\pi f_m(t-n\tau))]$ is a complex function characterizing the accumulated phase modulation in round trip l. The corresponding power spectrum consists of a frequency comb, in which the frequency of the m-th comb line is equal to $f_0 \pm mf_m$, with $m = 0, 1, 2\ldots$ (note that the central line, at $m = 0$, corresponds to the frequency of the CW seed laser).

To down-convert to the RF domain, the output electric field is mixed with the seed laser. Let us assume that the optical signal at the output of the loop is recombined with a fraction of the output of the CW seed laser, with an amplitude of $\beta E_{in}e^{-j\omega_o t}$. Then, the photocurrent due to the contribution of each individual optical waveform is written as

$$I = \left|\beta E_{in}e^{-j\omega_o t} + E_{out1}(t)\right|^2 \tag{3}$$

To limit the influence of intra-comb beatings, the optical power of the seed laser is much higher than the optical power at the FSL output ($\beta \gg 1$). Therefore, the resulting intensity is expressed as

$$I \propto \Re\left\{\sum_{l=1}^{N} p^l exp\left[jl\omega_o\tau + j\delta \sum_{n=1}^{l} \sin(2\pi f_m(t-n\tau))\right]\right\} E_{in}^2 \tag{4}$$

where $\Re$ denotes the real part. In the following, we will focus our discussion on the loop function $L(t)$, which is defined as

$$L(t) = \sum_{l=1}^{N} p^l exp\left[jl\omega_o\tau + j\delta \sum_{n=1}^{l} \sin(2\pi f_m(t-n\tau))\right] \tag{5}$$

Previous studies have investigated the properties of the phase-modulated FSLs under the integer Talbot and fractional Talbot conditions [23]. Here, we consider a special case in which the modulation frequency f_m is slightly detuned off an integer multiple of the fundamental loop frequency f_c, namely

$f_m = p'\ f_c + \Delta f$ (with p' being an integer and $\Delta f \ll f_c$)

$$\sin\left(2\pi f_m\left(t - n\tau\right)\right) = \sin\left(2\pi f_m t - 2n\pi\Delta f\tau\right) \tag{6}$$

Then, the loop function can be written as

$$L\ (t) = \sum_{l=1}^{N} p^l exp\left[jl\omega_o\tau + j\delta\sum_{n=1}^{l}\sin\left(2\pi f_m t - 2n\pi\Delta f\tau\right)\right]$$

$$= \sum_{l=1}^{N} p^l$$

$$exp\left[jl\omega_o\tau + \frac{j\delta sin\left(l\pi\Delta f\tau\right) sin\left(2\pi f_m t - \left(l+1\right)\pi\Delta f\tau\right)}{sin\left(\pi\Delta f\tau\right)}\right] \tag{7}$$

The spectral phase in Eq. (7) exhibits a sinusoidal dependence on the modulation frequency. The optical loop phase $e^{jl\omega_o\tau}$ is introduced by the seed laser. Different from the intensity-modulated FSL in which the optical phase exerts little influence on the output waveforms [23], [25], [26], the influence of the optical frequency on the phase-modulated FSL will be further investigated.

III. Sinusoidal Frequency-Modulated Waveform Pulse Doublets

To gain some physical insight into Eq. (7), we decompose $L(t)$ as follows:

$$L\ (t) = L_1\ (t) \times L_2\,(t) \tag{8}$$

with

$$L_1\ (t)\ =\ exp\left(-j\delta\frac{cos\left(2\pi f_m t - \pi\Delta f\tau\right)}{2sin\left(\pi\Delta f\tau\right)}\right)$$

$$L_2\ (t) = \sum_{l=1}^{N} p^l exp\left(jl\omega_o\tau + j\delta\frac{cos\left(2\pi f_m t - \left(2l+1\right)\pi\Delta f\tau\right)}{2sin\left(\pi\Delta f\tau\right)}\right) \tag{9}$$

We assume that $\pi\Delta f\tau$ is sufficiently small that the approximation $\sin\left(\pi\Delta f\tau\right) = \pi\Delta f\tau$ can be adopted. Then, $L_1(t)$ and $L_2(t)$ can be written as

$$L_1\ (t) = exp\left[-j\left(kcos\left(2\pi f_m t - \pi\Delta f\tau\right)\right)\right] \tag{10}$$

$$L_2\ (t) = \sum_{l=1}^{N} p^l exp\left[j\left(l\omega_o\tau + kcos\left(2\pi f_m t - \left(2l+1\right)\pi\Delta f\tau\right)\right)\right] \tag{11}$$

where $k = \delta/(2\pi\Delta f\tau)$ is a phase modulation index indicating the maximum phase offset. In the following, the simulation parameters are set as follows: $f_c = 10\ MHz$ ($\tau = 0.1\mu s$), the modulation depth is $\delta = \pi$ ($V = V_\pi$), the modulation frequency is adjusted to $f_m = f_c + \Delta f$ ($p' = 1$), and the number of round trips is fixed to $N = 500$. In addition, the intensity splitting ratio of the 2×2 coupler inside the loop is 50:50.

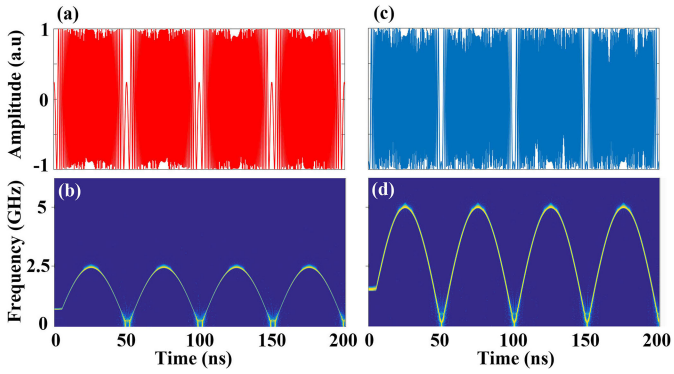

Fig. 2. Simulations of $L_1(t)$ with different modulation frequencies: (a)–(b) $f_m = 10.02$ MHz and (c)–(d) $f_m = 10.01$ MHz. The amplitudes in (a) and (c) represent the real part of $L_1(t)$, including negative values.

A. Behavior of $L_1(t)$

Analogous to wideband phase modulation, the instantaneous frequency of $L_1(t)$ can be written as

$$f_p = (1/2\pi)\, d\theta_1/dt\ =\ kf_m sin\left(2\pi f_m t - \pi\Delta f\tau\right) \tag{12}$$

where f_p is a sine function with a period of $1/f_m$. In contrast to a chirped waveform whose instantaneous frequency varies linearly with time, $L_1(t)$ is a continuous sinusoidal frequency-modulated (SFM) waveform. Notably, the average frequency of the SFM waveform in Eq. (10) is approximately zero, which means that the instantaneous frequency varies between $-kf_m$ and kf_m. In fact, to be physically meaningful, it should vary only from 0 to kf_m. The maximum frequency offset in one period is proportional to the product of the phase modulation index k and the modulation frequency f_m. The results of simulations performed with modulation frequencies of $f_m =$ 10.02 MHz ($k = 250$) and $f_m =$ 10.01 MHz ($k = 500$) are shown in Fig. 2. Note that the amplitudes (taking on negative values) plotted in Fig. 2(a) and Fig. 2(c) represent the real part of $L_1(t)$. Moreover, the short-time Fourier transform (STFT) is adopted to characterize the time-frequency characteristics of $L_1(t)$. The overlap parameter in the STFT is set to 0.99, which indicates that the data window slides along the time axis by a distance corresponding to only 1% of the points used in the calculation. As before, when the modulation frequency is 10.02 MHz, the instantaneous frequency varies sinusoidally from 0 to approximately 2.5 GHz ($k \times f_m$). With increasing k, the maximum frequency offset reaches approximately 5 GHz, as shown in Fig. 2(d). In addition, an instantaneous negative frequency is flipped to a positive frequency here, causing the period of the waveform to be halved.

B. Behavior of $L_2(t)$

$L_2(t)$ is the sum of a series of wideband phase-modulated signals with different phase shifts. The Jacobi-Anger expansion formula for the function $e^{jkcos\theta}$ is written as

$$e^{jkcos\theta} = \sum_{n=-\infty}^{+\infty} j^n J_n\left(k\right) e^{jn\theta} \tag{13}$$

where $J_n(k)$ is a Bessel function of order n. Replacing θ in the previous equation with $2\pi f_m t-(2l+1)\pi\Delta f\tau$ and inserting the result into the expression for the loop function in Eq. (11) leads to

$$\begin{aligned} L_2\ (t) = & \\ & \sum_{l=1}^{N} p^l exp\left[j\left(l\omega_o\tau + kcos\left(2\pi f_m t-(2l+1)\pi\Delta f\tau\right)\right)\right] \\ & = \sum_{n=-\infty}^{+\infty}\sum_{l=1}^{N} p^l j^n J_n\left(k\right) exp\left(jl\omega_o\tau\right) exp\left[jn\left(2\pi f_m t\right.\right. \\ & \left.\left. -(2l+1)\pi\Delta f\tau\right)\right] \end{aligned} \tag{14}$$

By using the geometric series formula, Eq. (14) can be rewritten as follows:

$$\begin{aligned} L_2\ (t) = & \sum_{n=-\infty}^{+\infty} j^n J_n\left(k\right) exp\left[jn\left(2\pi f_m t-\pi\Delta f\tau\right)\right] \\ & \sum_{l=1}^{N} p^l e^{jl\omega_o\tau} e^{-j2n\pi l\Delta f\tau} \\ = & \sum_{n=-\infty}^{+\infty} j^n J_n\left(k\right) exp\left[jn\left(2\pi f_m t-\pi\Delta f\tau\right)\right] M\left(n\right) \end{aligned} \tag{15}$$

where $M(n)$ is a complex function of n. In the limit of $N\to\infty$ and assuming $p<1$, the sum of the geometric series can be simplified to

$$M\ (n) = \frac{pexp\left(j\omega_0\tau - j2n\pi\Delta f\tau\right)}{1-pexp\left(j\omega_0\tau - j2n\pi\Delta f\tau\right)} \tag{16}$$

Evidently, $L_2(t)$ is a superposition of a series of high-order harmonics. In Eq. (15), the intensity of the harmonic of order n is the product of the Bessel function $J_n(k)$ and the complex function $M(n)$. $M(n)$ tends to be a periodic function with sharp peaks at the values of $\theta(n)$ given by $\theta\left(n\right)=\omega_0\tau-2n\pi\Delta f\tau = 2q\pi$ (where q is an integer). Benefiting from the periodicity of the sine function, $\omega_0\tau$ can be restricted to the range of 0 to 2π, i.e., $0\le\omega_0\tau-2p\pi\le 2\pi$. Then, the peak positions in $M(n)$ correspond to the harmonics of order n:

$$n\ = \left\lfloor\left(\omega_0\tau-2q\pi\right)/2\pi\Delta f\tau\right\rfloor, \tag{17}$$

where $\lfloor x\rfloor$ is no more than the integer part of x. As $\omega_0\tau$ increases from 0 to π, n increases from 0 to $1/(2\Delta f\tau)$. When $\omega_0\tau>\pi$, it presents the same value as in the case of $2\pi-\omega_0\tau$. Interestingly, the harmonic of order n ($n\times 2\pi f_m$) can be significantly enhanced due to the response of $M(n)$.

To illustrate the influence of the optical frequency on $L_2(t)$, we present simulations performed based on Eq. (15) with 6000 harmonics, $f_m=$ 10.01 MHz ($k=500$), and $p=0.97$. Fig. 3(a) depicts the simulation results obtained with $\omega_0\tau=\pi N/2$ (with N increasing from 0 to 3), showing that i) the response of $L_2(t)$ in the time domain is a pulse doublet and the interval between the two pulses strongly depends on $\omega_0\tau$, ii) the peak RF f_i is determined by $\omega_0\tau$. For example, when

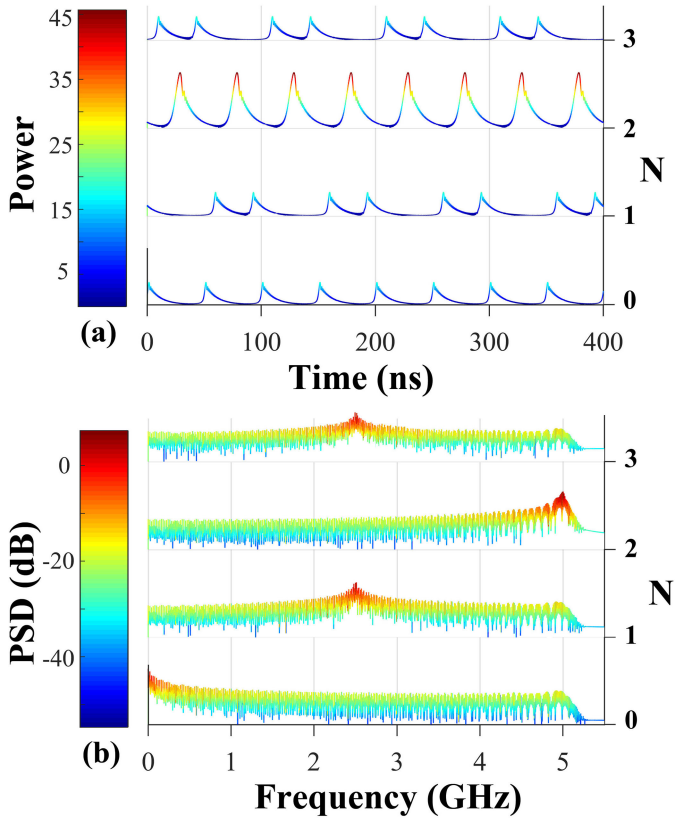

Fig. 3. Power (a) and power spectral density (b) of $L_2(t)$ with different optical phases $\omega_0\tau=\pi N/2$.

$\omega_0\tau=\pi/2$, n is calculated to be 250 and $f_i=$ 2.5025 GHz. Through a suitable analysis, f_i is found to be

$$f_i = \left\lfloor\left\{\left(\omega_0\tau-2q\pi\right)/2\pi\Delta f\tau\right\}\right\rfloor\times f_m \tag{18}$$

C. Intensity of the Output Waveform

According to the previous analysis, $L(t)$ can be decomposed as follows: $L\ (t)=L_1\ (t)\times L_2(t)$, where $L_1(t)$ and $L_2(t)$ represent a continuous SFM waveform and an RF-modulated pulse doublet waveform, respectively. Thus, we may predict that the final output waveform will consist of SFM pulse doublets and that the instantaneous frequency f_t of the loop function will be

$$f_t = \left|f_p+f_i\right| = \left|kf_m sin\left(2\pi f_m t-\pi\Delta f\tau\right)+f_i\right| \tag{19}$$

where f_p is the instantaneous frequency of $L_1(t)$, defined in Eq. (14), and f_i is the instantaneous frequency of $L_2(t)$, defined in Eq. (19). In this section, we will further investigate the time-frequency characteristics of $L(t)$.

1) SFM Pulse Doublets: From Eq. (7) and the definition of k, $L(t)$ can be written as

$$\begin{aligned} L\ (t) = & \sum_{l=1}^{N} p^l exp\left(jl\omega_o\tau + 2jksin\left(l\pi\Delta f\tau\right)\right. \\ & \left.\times\ sin\left(2\pi f_m t-\left(l+1\right)\pi\Delta f\tau\right)\right). \end{aligned} \tag{20}$$

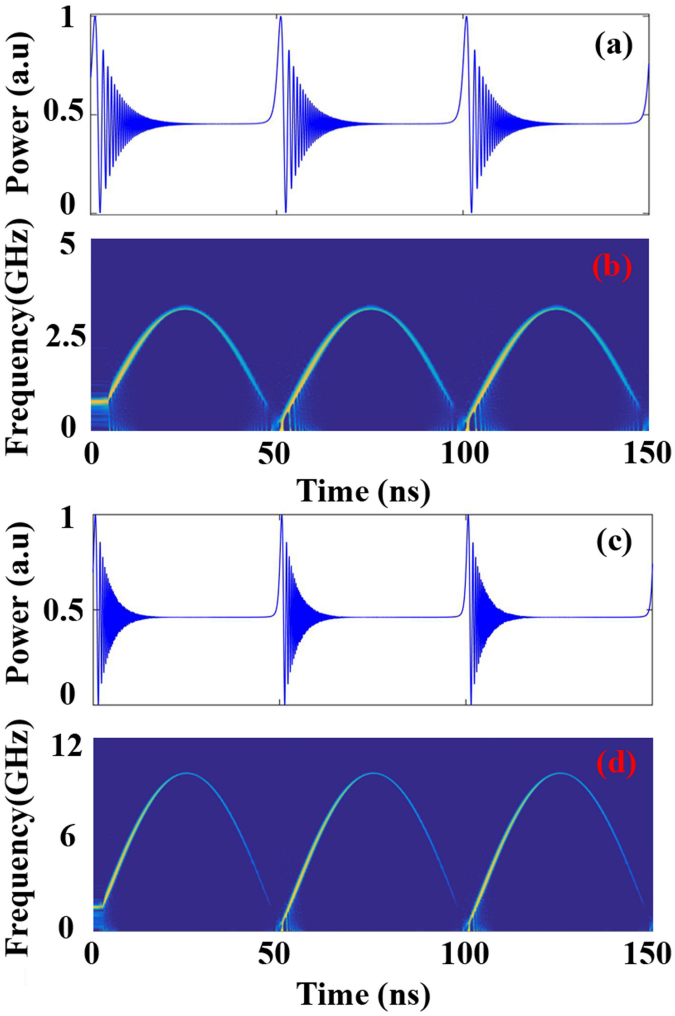

Fig. 4. Simulations of output power and STFT results with (a), (b) $\Delta f =$ 15 kHz (k = 333), and (c), (d) $\Delta f = 5$ kHz (k = 1000).

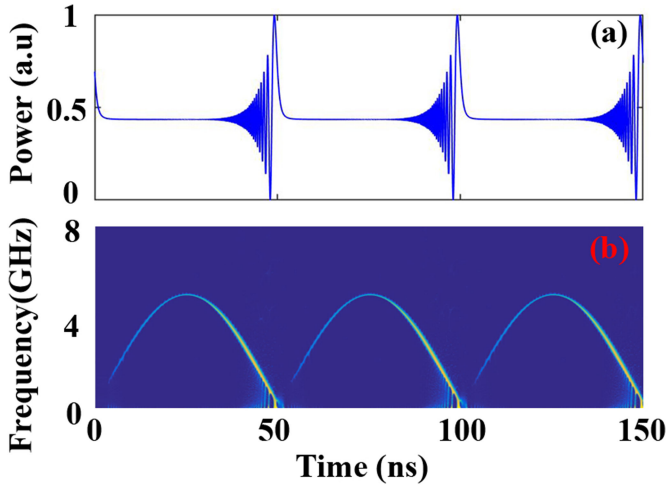

Fig. 5. Simulations of output power (a) and STFT (b) results with $\Delta f = -10\ kHz$ ($k = -500$).

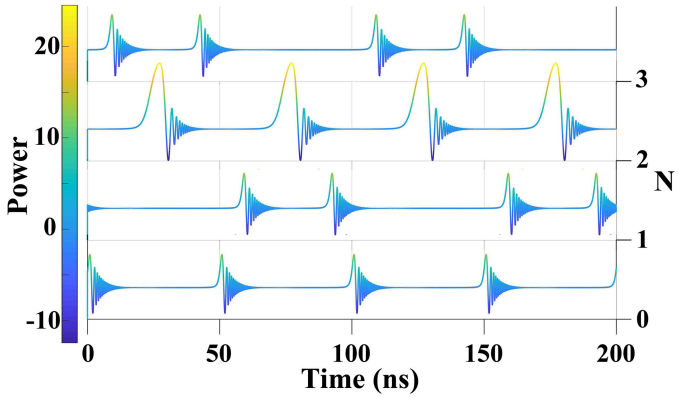

Fig. 6. Simulations of output power of $L(t)$ with different $\omega_0\tau = \pi N/2$.

When Δf is finite, the instantaneous phase of $L(t)$ in roundtrip l is

$$\theta_l = l\omega_o\,\tau + 2ksin\left(l\pi\Delta f\tau\right)sin\left(2\pi f_m t - (l+1)\,\pi\Delta f\tau\right) \tag{21}$$

where it follows a cosine function. Then, the instantaneous frequency is found to be

$$\begin{aligned} f_l &= (1/2\pi)\,d\theta_l/dt \\ &= 2kf_m sin\left(l\pi\Delta f\tau\right)cos\left(2\pi f_m t - (l+1)\,\pi\Delta f\tau\right) \end{aligned} \tag{22}$$

We present simulations performed based on Eq. (20) with $\Delta f = 15$ kHz and 5 kHz, and with the other parameters set to $\omega_o\tau = 0, p = 0.97$ and $N = 500$. The output time traces and the corresponding STFT plots are shown in Fig. 4. As shown in Fig. 4(a) and (c), an optically carried RF pulse with a repetition rate equal to twice the modulation frequency f_m is observed in the time domain.

To evaluate the instantaneous frequency properties with time, we also present the STFT results for simulations of Eq. (21) in Fig. 4, demonstrating that the instantaneous frequency of the optically carried RF pulses varies sinusoidally with time. When the modulation frequency is $f_m =$ 10.005 MHz, the maximum frequency offset reaches 10 GHz. Because $\omega_0\tau = 0$, namely, $f_i = 0$, the maximum RF offset is equal to f_p: the product of the modulation frequency f_m and the phase modulation index k. We then investigate the influence of the sign of Δf on the output waveform for this PM-FSL. We present simulations performed with $\Delta f = -10$ kHz in Fig. 5. As shown in Fig. 5(a) and 5(b), the SFM pulse doublets exhibit a half-period shift in the time domain, and the intensity and instantaneous frequency both present the opposite properties compared with the results for positive Δf.

2) Influence of the Optical Frequency on the Waveform: In the previous section, the optical frequency was set to $\omega_0\tau = 0$. However, the optical frequency will be subject to a phase accumulation ($l\omega_o\tau$) in round trip l, which will lead to a frequency offset of the SFM pulse doublets. To demonstrate the influence of the optical frequency on the output waveform, we adopt a fixed $\Delta f = 10\ kHz$ and simulate the loop function with various values of $\omega_0\tau = \pi N/2$ (with N increasing from 0 to 3). As shown in Fig. 6, the interval between the two pulses strongly depends on $\omega_0\tau$, and the delay corresponds to a half-period shift when $\omega_0\tau = \pi$.

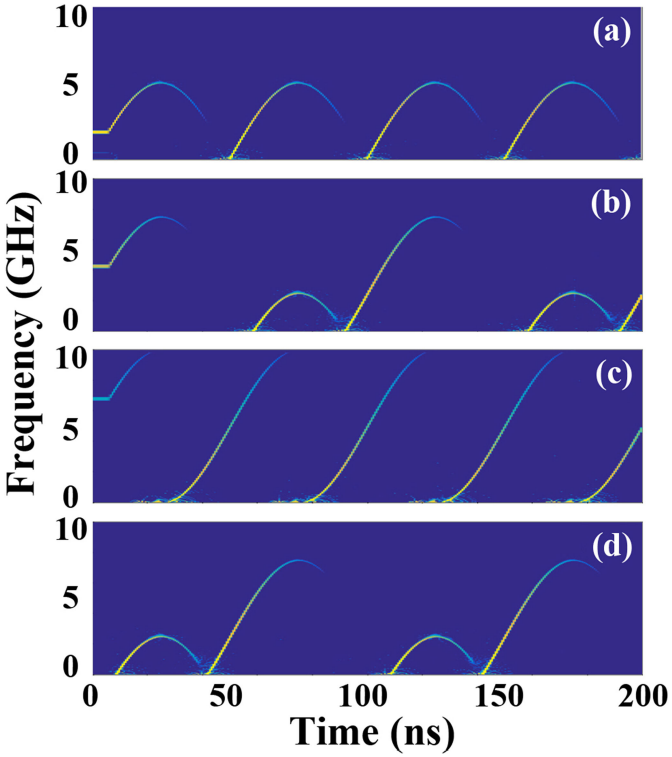

Fig. 7. Time-frequency distributions of $L(t)$ with (a) $\omega_0\tau = 0$, (b) $\omega_0\tau = \pi/2$, (c) $\omega_0\tau = \pi$, (d)$\omega_0\tau = 3\pi/2$.

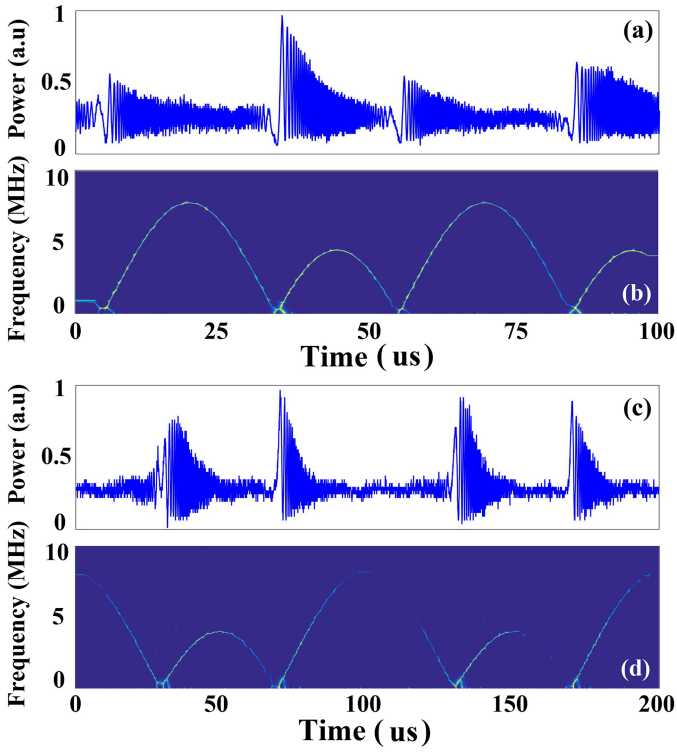

Fig. 8. Experimental results of sinusoidal frequency modulation pulse doublet with (a, b) $f_m = 20$ kHz and (c, d) $f_m = 10$ kHz. (a), (c): Temporal waveforms; (b), (d) calculated STFT of the measured waveforms.

We now analyze the time-frequency distributions of the waveforms. The simulation parameters are the same as in the setting considered in Fig. 6. The overlap parameter in the STFT is 0.99. We present time-frequency simulations performed with $\omega_0\tau = \pi N/2$ (with N increasing from 0 to 3) in Fig. 7(a)–(d), respectively. In this simulation, kf_m is fixed to approximately $5\ GHz$. As $\omega_0\tau$ increases from 0 to π, the RF f_i also increases from 0 to kf_m. Notably, because $f_i \leq kf_m$, the instantaneous frequency is divided into two parts due to the absolute value representation. For example, when $\omega_0\tau = \pi/2$, f_i is calculated to be $2.5\ GHz$ (as shown in Fig. 3(b)). The instantaneous frequency f_t will start from approximately $2.5\ GHz$ (at $t = 0$, $sin(2\pi f_m t - \pi\Delta f\tau) \approx 0$), and for a certain period of time, $kf_m sin(2\pi f_m t - \pi\Delta f\tau) + f_i$ will take a negative value and will mirror the behavior shown on the positive frequency axis in Fig. 7(b). When $\omega_0\tau = \pi$, f_i is $5\ GHz$. The instantaneous frequency will vary between $0\ Hz$ and $10\ GHz$, as shown in Fig. 7(c). However, when $\omega_0\tau > \pi$, the instantaneous frequency is the same as in the case of $2\pi - \omega_0\tau$ but with a half-period shift.

IV. Experiment Results

We conduct an experiment to demonstrate the ability of the proposed scheme to generate SFM pulses. The seed is a fiber-coupled single-frequency laser designed with nonplanar ring oscillator that delivers 1 mW at 1064 nm, with a linewidth of approximately 10 kHz. The components described in this section are presented in Fig. 1. The bandwidth of the TBPF in the loop is 0.35 nm and the loop round-trip frequency presents high stability that is measured to be $f_c = 14.586483$ MHz in the mode-locking regime. To improve the stability, the loop is designed with all-polarization fiber components and the experiments are conducted in a relatively closed box to isolate the system from the acoustic and thermal effects. Thus, $\omega_0\tau$ is considered to be a constant value over a period of time. The phase modulator in the experiment is an EOPM with a 10 GHz-bandwidth and 18 V half-wave voltage at 50 kHz. The peak-to-peak RF voltage applied to the EOPM remains 15 V. The center frequency of the TBPF is fixed to match the frequency of the seed laser. In the experiment, the pump current of the YDFA is adjusted to increase the gain coefficient in the loop while avoiding parasitic oscillation. The detection setup consists of a 5 GHz bandwidth photodiode and an 8 GHz bandwidth oscilloscope.

To demonstrate the potential of the proposed technique for the generation of SFM pulse doublets with configurable values of the repetition rate and bandwidth, we perform measurements with different values of modulating frequency. A short-time Fourier transformation is performed to obtain the instantaneous frequency. The obtained time traces, measured after recombination with the seed laser, and the corresponding STFT plots are shown in Figs. 8 and 9. In line with the theoretical results obtained with $f_m = p'\, f_c + \Delta f$ (where p' is an integer and $\Delta f \ll f_c$), the time response of the phase-modulated FSL in the small detuning case consists of SFM pulse doublets with a repetition rate equal to the RF frequency applied to the EOPM. Figs 8(a)–(d) report the experimental results for $f_m = 20$ kHz and 10 kHz ($p' = 0$), respectively. According to the theoretical analysis, the instantaneous frequency is divided into two parts due to the absolute

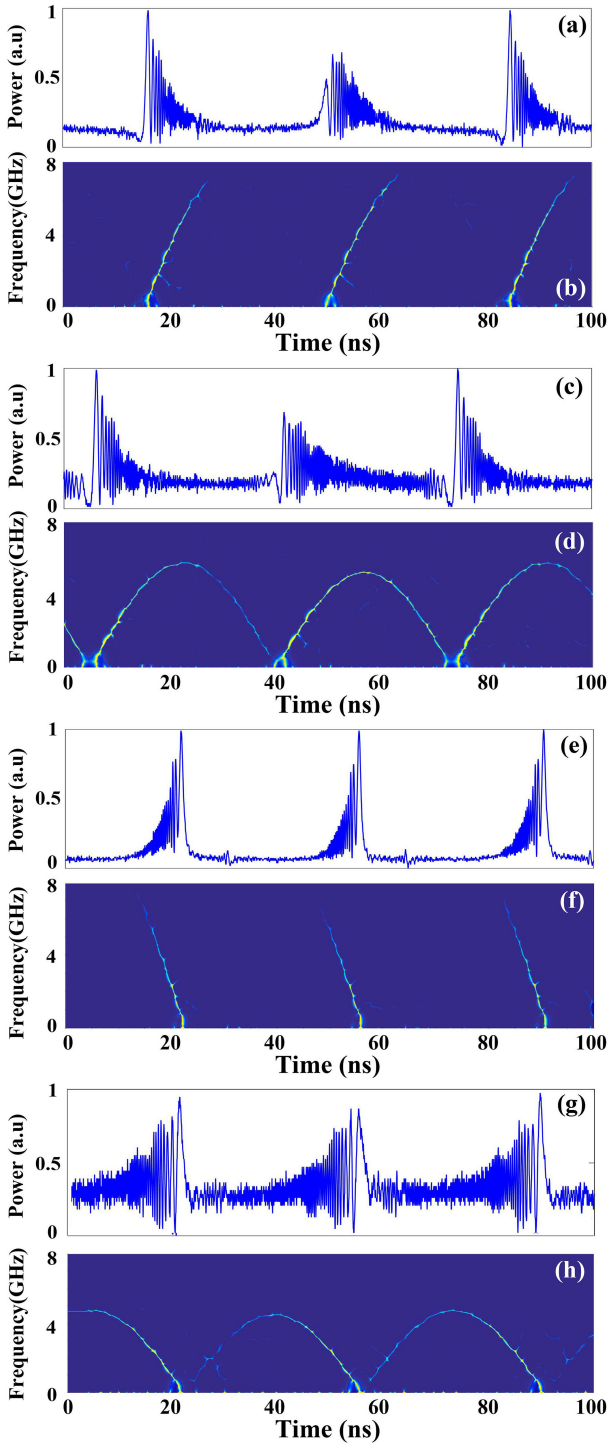

Fig. 9. Experiment results of sinusoidal frequency modulation pulse doublet with (a, b) $f_m = f_c + 10$ kHz (c, d) $f_m = f_c + 15$ kHz , (e, f) $f_m = f_c - 10$ kHz, (g, h) $f_m = f_c - 20$ kHz. (a), (c), (e), (g): Temporal waveforms; (b), (d), (f), (h), calculated STFT of the measured waveforms.

value representation. The measured "peak-to-peak" amplitude of the sinusoidal function in Fig. 8(b) is 12.4 MHz (7.7 MHz + 4.7 MHz), which is slightly lower than the theoretical value $f_{BW} = k \times f_m = 14.86$ MHz. The difference occurs because the RF power applied to the EOPM in the experiment is less than the half-wave voltage.

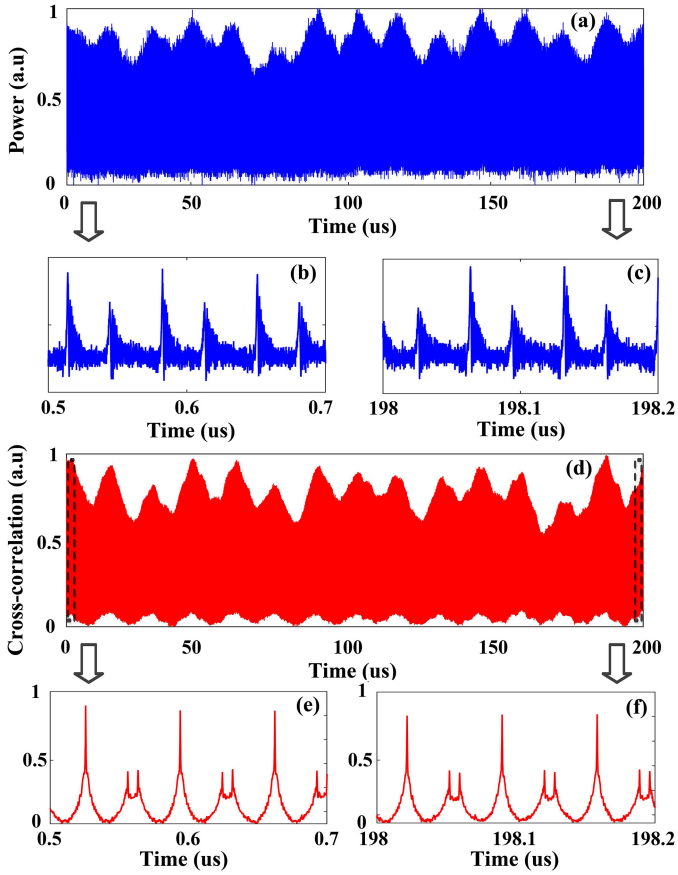

Fig. 10. Stability of SFM waveforms. (a) temporal trace with duration of 200 μs; (b)-(c) temporal traces with a duration of 0.2 μs for the delay times of 0.5 μs and 198 μs; (d) Cross-correlation trace for the duration of 20 0 μs; (e) and (f) Cross-correlation coefficient with the temporal delays of 0.5 μs and 198 μs.

To demonstrate the generated SFMs with reconfigurable bandwidth and repetition rate, we perform measurements by tuning the RF in the vicinity of the round-trip frequency. As shown in Figs. 9(a) and 9(b), in which the modulating frequency is set to $f_m = f_c + 10$ kHz ($p' = 1$, $\Delta f = 10$ kHz), the waveforms in the time-frequency domain are SFM pulse doublets, and the "peak-to-peak frequency" reaches 14.4 GHz (7.1 GHz + 7.3 GHz), which is limited by the detection bandwidth of the photodiode. It is worthwhile to note that the "peak-to-peak frequency" should be approximately 20 GHz. By simply increasing the RF applied to the EOPM to $f_m = f_c + 15$ kHz, it is decreased to 10.7 GHz (5.6 $GHz + 5.1$ GHz), as shown in Figs. 9(c) and 9(d). By simply tuning the input RF tone over a span of a few kHz in the vicinity of f_c, we observe the SFM pulse doublets with a bandwith of 7.3 GHz (approximately half of the peak-to-peak value). Finally, we investigate the case in which Δf is negative. Fig. 9(e)–9(h) report the experimental results when $f_m = f_c - 10kHz$ and $f_m = f_c - 20kHz$, respectively. As shown in Fig. 9(e)–9(h), the instantaneous frequency shows the opposite trend to the positive results for Δf. It is important to note that the ratio of the time delays of the SFM pulse-doublet and the modulation period depends on $\omega_0 \tau$. As illustrated in

Figs. 8 and 9, the ratio values are different mainly due to the slow frequency drift of the seed laser.

Then, we investigate the stability of the generated waveforms. The modulation frequency is set to $f_m = f_c + 30$ kHz and a time trace with a duration of 200 μs is recorded (limited by the record length of the oscilloscope). As shown in Fig. 10(a), the intensity fluctuates with time mainly due to the power fluctuation of the seed laser. As observed from Figs. 10(b) and (c), the two sequences extracted at the different delay times of 0.5 μs and 198 μs show similar patterns. To further characterize the loop stability, an individual trace is numerically extracted from the sequence, and used as a reference to calculate the cross-correlation of all of the individual waveforms. The cross-correlation trace displayed in Fig. 10(d) show a similar intensity fluctuation envelope. Additionally, the auto-correlation peak width at the delay times of 0.5 μs and 198 μs are almost identical, demonstrating the high stability of the generated SFMs, as shown in Figs. 10(e) and (f). The time sidebands are caused by the correlation property of the SFM pulse-doublets in a single modulating period.

V. Conclusion

We have proposed and experimentally demonstrated a phase-modulated FSL for the generation of SFM waveforms. This experiment shows an alternative approach to AOFS loops, taking advantage of the inherent bandwidth and tunability of the EOPM. In contrast to AOFS-based FSL approaches, our scheme only uses one EOPM driven by a low-frequency signal from kHz to MHz to generate SFM waveforms with bandwidth from MHz to GHz. In addition, EOPMs are much easier to integrate with other fibered devices. All of these result in significant improvements in terms of reducing the complexity, size, weight and related potential costs of the system as well as increasing the stability and flexibility.

Compared with the traditional linear chirped waveforms, the waveforms we evidenced present sinusoidal frequency modulation. To the best of our knowledge, this is the first demonstration of phase-modulated FSL in generating SFM waveforms. Moreover, the SFM waveforms are easily configured to different repetition rates and bandwidth by simply tuning the modulating frequency. In our case, we have demonstrated SFM waveforms with bandwidth of greater than 7 GHz range by just tuning the input RF tone over a span of a few kHz in the vicinity of f_c. This value could be further increased or decreased by adjusting the modulating frequency and the FSL loop length. As shown in Fig. 8, implementing an FSL with a modulation frequency of 20 kHz ($p' = 0$) would enable the generation of SFM with bandwidth MHz range. On the other hand, generating waveforms with much wider bandwidth can be achieved by simply increasing the value of the modulating frequency, benefiting from the high bandwidth of the EOPM (dozens of GHz). It is worthwhile to note that the bandwidth of the SFM waveforms we report is limited by the photodiode bandwidth. By employing a faster photodetector and properly setting the modulating frequency in the GHz range, the fiber-optics platform demonstrated in our work would enable the generation of SFM waveforms with a bandwidth above the THz scale. As stated above, the repetition rate is equal to the RF frequency applied to the EOPM. In our case, we have demonstrated waveforms with tunable repetition rate by tuning the RF in the vicinity of 10 kHz ($p' = 0$) and 14.5 MHz ($p' = 1$). The repetition rate can be increased merely by tuning the modulating frequency with larger p'.

Based on the potential future upgrades, the presented concept could be extended to integrated photonics since optical rings, filters, and EOPMs can be integrated on photonic platforms. This work is expected to have significant implications in the domains of radar, RF signal processing and communications. For example, in pulse compression radar, the possibility to transmit SFM pulses with a large time-bandwidth product would significantly enhance the sensitivity of radar systems and enable instantaneous and simultaneous measurements of distance and velocity by matched filtering [5], [19].

Acknowledgment

The authors thank Prof. Marc BRUNEL (University of Rennes 1, France) and Prof. Marc VALLET (University of Rennes 1, France) for fruitful discussions.

References

[1] E. C. Farnett, G. H. Stevens, and M. Skolnik, "Pulse compression radar," *Radar Handbook*, vol. 2, pp. 10–11, 1990.
[2] J. L. Neill, B. J. Harris, A. L. Steber, K. O. Douglass, D. F. Plusquellic, and B. H. Pate, "Segmented chirped-pulse fourier transform submillimeter spectroscopy for broadband gas analysis," *Opt. Exp.*, vol. 21, no. 17, pp. 19743–19749, 2013.
[3] S. Pan and J. Yao, "Photonics-based broadband microwave measurement," *J. Lightw. Technol*, vol. 35, no. 16, pp. 3498–3513, 2016.
[4] D. Tse and P. Viswanath, *Fundamentals of Wireless Communication*, Cambridge, MA, USA: Cambridge Univ. Press, 2005.
[5] J. M. Kurdzo, B. L. Cheong, R. D. Palmer, and G. Zhang, "Optimized NLFM pulse compression waveforms for high-sensitivity radar observations," in *Proc. Int. Radar Conf.*, Lille, France, Oct. 2014, pp. 1–6.
[6] R. Ghavamirad, H. Babashah, and M. A. Sebt, "Nonlinear FM waveform design to reduction of sidelobe level in autocorrelation function," in *Proc. Iranian Conf. Elect. Eng.*, Tehran, Iran, May 2017, pp. 1973–1977.
[7] J. Capmany, G. Li, C. Lim, and J. Yao, "Microwave photonics: Current challenges towards widespread application," *Opt. Exp.*, vol. 21, no. 19, pp. 22862–22867, 2013.
[8] A. Rashidinejad, Y. Li, and A. M. Weiner, "Recent advances in programmable photonic-assisted ultrabroadband radio-frequency arbitrary waveform generation," *IEEE J. Quantum Electron*, vol. 52, no. 1, pp. 1–17, Jan. 2016.
[9] Z. Tang, Y. Li, J. Yao, and S. Pan, "Photonics-Based microwave frequency mixing: Methodology and applications," *Laser Photon. Rev.*, vol. 14, no. 1, 2020, Art. no. 1800350.
[10] H. P. Bazargani and J. Azaña, "Optical pulse shaping based on discrete space-to-time mapping in cascaded co-directional couplers," *Opt. Exp.*, vol. 23, no. 18, pp. 23450–23461, 2015.
[11] C. Wang and J. Yao, "Large time-bandwidth product microwave arbitrary waveform generation using a spatially discrete chirped fiber bragg grating," *J. Lightw. Technol*, vol. 28, no. 11, pp. 1652–1670, 2010.
[12] D. E. Mittelberger, R. D. Muir, M. Y. Hamamoto, M. A. Prantil, and J. E. Heebner Mittelberger, "Frequency-to-time optical arbitrary waveform generator," *Opt. Lett*, vol. 44, no. 11, pp. 2863–2866, 2019.
[13] A. M. Weiner, "Ultrafast optical pulse shaping: A tutorial review," *Opt. Commun*, vol. 284, no. 15, pp. 3679–3692, 2011.
[14] A. Dezfooliyan and A. M. Weiner, "Photonic synthesis of high fidelity microwave arbitrary waveforms using near field frequency to time mapping," *Opt. Exp.*, vol. 21, no. 19, pp. 22974–22987, 2013.
[15] Y. Chen and S. Pan, "Simultaneous wideband radio-frequency self-interference cancellation and frequency down conversion for in-band full-duplex radio-over-fiber systems," *Opt. Lett.*, vol. 43, no. 13, pp. 3124–3127, 2018.

[16] P. Tovar, Luis E. Y. Herrera, M. R. Ribeiro, and J. P. V. D. Weid, "Photonic generation of NLFM microwave pulses from DFB-laser chirp," *IEEE Photon. Technol. Lett.*, vol. 31, no. 17, pp. 1417–1420, Sep. 2019.
[17] H. Guillet de Chatellus, L. Romero Cortés, C. Schnébelin, M. Burla, and J. Azaña, "Reconfigurable photonic generation of broadband chirped waveforms using a single CW laser and low-frequency electronics," *Nat. Commun.*, vol. 9, no. 1, pp. 1–12, 2018.
[18] H. Yang, M. Brunel, H. Zhang, M. Vallet, C. Zhao, and S. Yang, "RF up-conversion and waveform generation using a frequency-shifting amplifying fiber loop, application to doppler velocimetry," *IEEE Photon. J.*, vol. 9, no. 6, pp. 1–9, Dec. 2017.
[19] J. Clement, C. Schnébelin, H. Guillet de Chatellus, and C. Fernández-Pousa, "Laser ranging using coherent pulse compression with frequency shifting loops," *Opt. Exp.*, vol. 27, no. 9, pp. 12000–12010, 2019.
[20] H. Yang, C. Zhao, H. Zhang, Z. Zhang, and K. Gui, "A novel hybrid TOF/phase-shift method for absolute distance measurement using a falling-edge RF-modulated pulsed laser," *Opt. Laser Technol.*, vol. 114, pp. 60–65, 2019.
[21] L. P. Yatsenko, B. W. Shore, and K. Bergmann, "Theory of a frequency-shifted feedback laser," *Opt. Commun.*, vol. 236, nos. 1-3, pp. 183–202, 2004.
[22] H. Guillet de Chatellus, E. Lacot, W. Glastre, O. Jacquin, and O. Hugon, "Theory of talbot lasers," *Phys. Rev.*, vol. 88, no. 3, 2013, Art. no. 033828.
[23] H. Yang, M. Brunel, M. Vallet, H. Zhang, and C. Zhao, "Analysis of frequency-shifting loops in integer and fractional talbot conditions: Electro-optic vs acousto-optic modulation," *J. Opt. Soc. Amer. B*, vol. 37, no. 11, 2020, Art. no. 3162-3169.
[24] F. Tian, X. Zhang, J. Li, and L. Xi, "Generation of 50 stable frequency-locked optical carriers for tb/s multicarrier optical transmission using a recirculating frequency shifter," *J. Lightw. Technol*, vol. 29, no. 8, pp. 1085–1091, 2011.
[25] H. Yang, M. Vallet, H. Zhang, C. Zhao, and M. Brunel, "Pulse doublets generated by a frequency-shifting loop containing an electro-optic amplitude modulator," *Opt. Exp.*, vol. 27, no. 13, pp. 18766–18775, 2019.
[26] H. Yang, M. Brunel, M. Vallet, C. Zhao, H. Zhang, and L. WANG, "Temporal talbot effect using an intensity-modulating frequency-shifting loop," in *Proc. SPIE*, 2020, Art. no. 113542G.

Hongzhi Yang was born in 1990, in Shanxi, China. He received the B.S. and Ph.D. degrees from the Beijing institute of Technology, Beijing, China, in 2013 and 2019, respectively. He joined Qian Xuesen Laboratory, the Academy of Space Technology, Beijing, China, in 2019. His research interests include microwave photonics and lidar-radar detection.

Lei Wang received the Ph.D. degree from the Beijing institute of Technology, Beijing, China, in 2013. He joined Qian Xuesen Laboratory, the Academy of Space Technology, Beijing, China, in 2013. His research interests include laser physics and lidar detection.

Changming Zhao received the B.S. degree from the University of Science and Technology of China, Hefei, China, in 1983 and the Ph.D. degree from Tianjin University, Tianjin, China, in 1993. From 1994 to 1995, he was a Postdoctoral Fellow with the School of Optics and Photonics, Beijing institute of Technology, Beijing, China. Since 1995, he has been with the Beijing Institute of Technology. His research interests include solar-pumped solid-state laser and lidar-radar detection.

Haiyang Zhang received the B.S. and Ph.D. degrees from the Beijing institute of Technology, Beijing, China, in 2004 and 2009, respectively. Since 2009, he has been with the Beijing institute of Technology. His research interests include remote sensing and microwave photonics.